Biomechanical Modeling of the Prostate for Procedure Guidance and Simulation

S. E. Salcudean, R. S. Sahebjavaher, O. Goksel, A. Baghani, S. S. Mahdavi, G. Nir, R. Sinkus and M. Moradi

Abstract Biomechanical models of the prostate have a number of potential applications in the diagnosis and management of prostate cancer. Most importantly, it has been shown in several studies that cancerous prostate tissue has different viscoelastic properties than normal prostate tissue: it is typically stiffer (higher storage modulus) and more viscous (higher loss modulus). If a strong correlation can be obtained between malignant tissue and its viscoelastic properties, then all commonly practiced prostate cancer procedures—biopsies, surgery and radiation treatment—can be improved by elasticity imaging. The elastic properties of the prostate and peri-prostatic tissue can also be used in procedure planning, even if such elastic properties do not show strong correlation to cancer. This chapter starts with an introduction to the prostate anatomy, prostate cancer, and a description of the most common procedures and their clinical needs. It continues by presenting the potential impact of elasticity imaging on these procedures. A brief survey of elastography techniques is presented next, with a sampling of some prostate elastography results to date. We describe two of the systems that we developed for the acquisition of prostate ultrasound and magnetic resonance elastography images and summarize our results to date. We show that

S. E. Salcudean (✉) · R. S. Sahebjavaher · A. Baghani · S. S. Mahdavi · G. Nir · M. Moradi
Department of Electrical and Computer Engineering, University of British Columbia, Vancouver, Canada
e-mail: tims@ece.ubc.ca

O. Goksel
Computer Vision Laboratory, Eidgenössische Technische Hochschule, Sternwartstrasse 7, 8092 Zürich, Switzerland

R. Sinkus
Centre de Recherche Biomédicale Bichat-Beaujon, U773, CRB3, Hôpital Beaujon, Clichy, France

Stud Mechanobiol Tissue Eng Biomater (2012) 11: 169–198
DOI: 10.1007/8415_2012_121
© Springer-Verlag Berlin Heidelberg 2012
Published Online: 19 February 2012

these elasticity images can be used for prostate segmentation and cross-modality image registration. Furthermore, we show how prostate region deformation models can be used in the development of a prostate brachytherapy simulator which can also be used in the planning of needle insertions that account for deformation.

1 Introduction

1.1 Prostate Anatomy

The prostate is a walnut size glandular organ located inferior to the bladder and anterior to the rectum (see Fig. 1). The urethra is a channel through the prostate that connects the bladder to the urethral sphincter at the base of the penis and allows urine to flow. Part of the semen which is stored with the sperm in the seminal vesicles is produced by the prostate. The seminal vesicles are connected to the urethra through the ejaculatory ducts. These ducts and the urethra form an approximate pyramidal shape with curved edges (see Fig. 1). As illustrated in this figure, the prostate has four zones. The transition zone surrounds the urethra close to the intersection of the urethra with the ejaculatory ducts. The central zone of the prostate surrounds the ejaculatory ducts and extends to the transition zone and the urethra superior to the transition zone. The peripheral zone surrounds the central and transition zones. This zone forms roughly three quarters of the prostate. Anteriorly, the peripheral zone is bounded by an anterior fibromuscular stroma zone. The superior part of the prostate adjacent to the bladder is called the base. At the base, the prostate peripheral zone has predominantly smooth muscle cells and blends into the bladder neck. The inferior part of the prostate is called the apex and is rich in striated muscle, and blends into the muscle of the pelvic diaphragm. See [1, 2] for excellent discussions of the prostate anatomy.

1.2 Prostate Cancer

Prostate cancer is the most common malignancy affecting North-American men. It is estimated that over one quarter million new cases will be diagnosed in North America in 2011, and that over 40,000 men will die of the disease in the same year [3]. In its early stages, prostate cancer has no symptoms and it is usually suspected when a prostate-specific antigen (PSA) test has shown a significant increase and/or when a digital rectal examination (DRE) shows stiff nodules or an asymmetric gland. Most prostate cancer occurs in the peripheral zone of the prostate, followed by the transition zone, then by the central zone. Diagnosis cannot be confirmed until a biopsy test is returned positive. Prostate cancer is multi-focal in nature, although recent studies have shown that in many cases there is one focal region responsible for cancer growth [4].

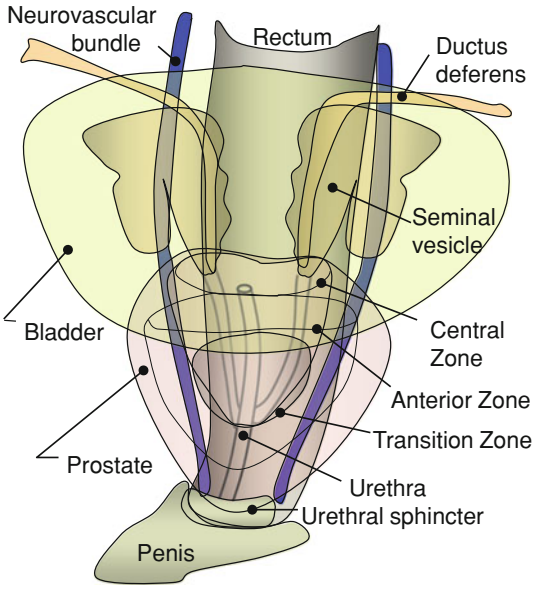


Fig. 1 Prostate rendering with major anatomical landmarks, including an outline of internal prostate anatomy and zones

1.3 Prostate Cancer Interventions

There are three major classes of interventions related to prostate cancer: prostate biopsy, radical prostatectomy and radiation treatment.

1.3.1 Prostate Biopsy

Prostate biopsies are performed with trans-rectal ultrasound (TRUS) guidance with the patient in the lateral decubitus or dorsal lithotomy position. Tissue cores are obtained with an end-firing convex TRUS transducer that has a needle guide attached to it (see Fig. 2).

While the prostate can be contoured with some confidence in B-mode ultrasound, such imaging is not accurate enough to reliably detect cancer. Nevertheless palpable tumors by DRE can often be seen to be hypoechoic in B-mode ultrasound. The false-negative rate of a TRUS-guided, multiple site biopsy procedure is 33–40% and cancer detection rates on first biopsy are as low as 25–36% [5, 6]. The addition of Doppler imaging does not significantly increase the accuracy of cancer detection; it has been shown that prostate pathologies can show low, moderate or high vascularity based on measured flow, regardless of whether they are cancerous or not.

Because prostate cancer cannot be reliably imaged under ultrasound, the goal of current standard-of-care ultrasound-guided biopsy protocols is to sample the entire prostate. Samples are taken primarily in the peripheral area of the gland, in the

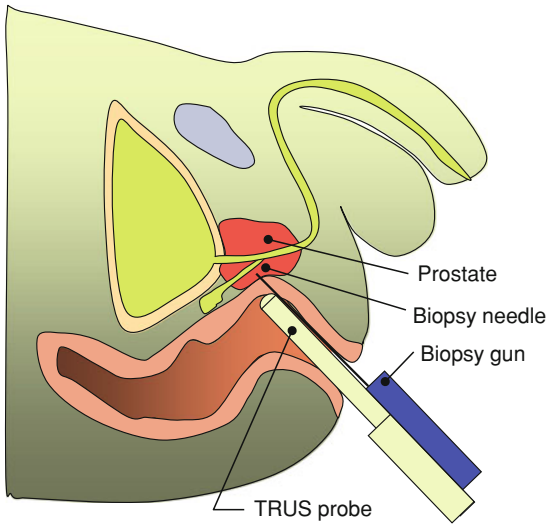


Fig. 2 End-firing TRUS with biopsy gun attached to it sampling the peripheral zone of the prostate

apex, mid-gland and base regions, left and right. There are many protocols but most take between 6 and 12 tissue cores. The distribution of samples is difficult to assess because it is difficult to precisely orient the transducer plane relative to the prostate volume. Systems that use external trackers [7] and registration to previously taken ultrasound images [8] have been developed to guide the random sampling of the prostate and to keep a record of where the samples have been taken from. Systems for performing prostate biopsy and brachytherapy directly under MRI guidance have also been developed, but these are not in common clinical use yet [9]. Alternatively, there are some existing systems that attempt to use intra-procedure registration of ultrasound to pre-operative MRI [8].

1.3.2 Radical Prostatectomy

Most of the prostate surgeries in North America are robot-assisted procedures carried out using the da Vinci® robot (Intuitive Surgical Inc., Sunnyvale, CA), with the patient in lithotomy position. A typical surgery takes place as summarized next.

A Foley catheter is inserted through the penis into the bladder, then trocars are placed in the abdomen and the abdomen is insufflated. The arms of the da Vinci® system are used to position a camera and instruments through the trocars into the patient. During the surgery, a bloodless field is achieved first by suture ligating the dorsal venous complex near the base of the prostate. Dissection of the bladder neck proceeds until the urethra and the catheter within it are visualized. The posterior wall of the bladder neck is dissected to reach and expose the seminal vesicles. A posterior rectal surgical plane is developed towards the urethral sphincter.

For nerve sparing procedures, the neurovascular bundle is released from the prostate. The urethra is divided from the prostate apex, leaving a urethral stump. The prostate and the seminal vesicles are removed. A vesico-urethral anastomosis is performed by suturing the bladder neck over the urethral stump.

There have been several studies that have shown that TRUS guidance during radical prostatectomy can be beneficial. In particular, TRUS guidance can be used to aid in identifying the correct surgical plane between the bladder neck and the prostate base, especially for novice robotic surgeons, to ensure a complete and accurate dissection of the prostate apex, and to help preserve an adequate urethral stump [10–12]. Monitoring surgical tool position relative to the prostate capsule to avoid accidental capsulotomy has also been mentioned as being beneficial.

1.3.3 Brachytherapy

Brachytherapy is often offered to suitable patients with localized prostate cancer as an alternative to radical prostatectomy [13]. The low-dose rate version of the treatment consists of the placement of small radioactive sources in the prostate using trans-perineal insertion of needles, in a pattern that delivers a sufficient radiation dose to kill the cancer while maintaining a tolerable dose to the urethra, bladder and rectum (Fig. 3). In a typical North-American approach, the procedure takes place a few weeks after a "volume study" of the patient's prostate is acquired. A sequence of transverse B-mode TRUS images acquired at different transdcer insertion depth are segmented to create a 3D geometric model of the prostate. Based on this geometric model, a medical physicist generates a treatment plan. The plan consists of individual seed locations placed at different depths along a number of parallel lines - the planned needle insertions. The procedure is carried out a few weeks later under general or spinal anesthesia. To begin with, the physician—a radiation oncologist or a urologist—manually aligns the TRUS, using US images, so that the pre-operative and intra-operative ultrasound images are registered to each other. This is done by using the coarse and fine adjustments of a brachytherapy stabilizer such as the Micro-Touch device (CIVCO Medical Solutions, Kalona, Iowa). The physician adjusts the TRUS depth and angle relative to the prostate by using a "stepper" unit (e.g., CIVCO EXII, CIVCO Medical Solutions) mounted onto the stabilizer. An insertion template is attached to the stepper. The template has a rectangular array of guiding holes. The radiation oncologist uses the guiding template, which has coordinate labels on it, to insert each needle to the planned coordinates, then pulls the needles out, leaving the seeds in the prostate. Typically, he or she inserts 80–130 seeds with 20–35 needles. The procedure relies upon real-time TRUS imaging to ensure the needle tip is inserted at the planned coordinates. Fluoroscopic anterior-posterior projections are acquired to show a 2D projection of the implanted seeds. In low-dose rate brachytherapy, the sources remain in the patient and the radiation lasts a few months.

The high-dose version of the treatment involves the planned insertion of highly radioactive sources into the prostate through catheters. The location of the sources

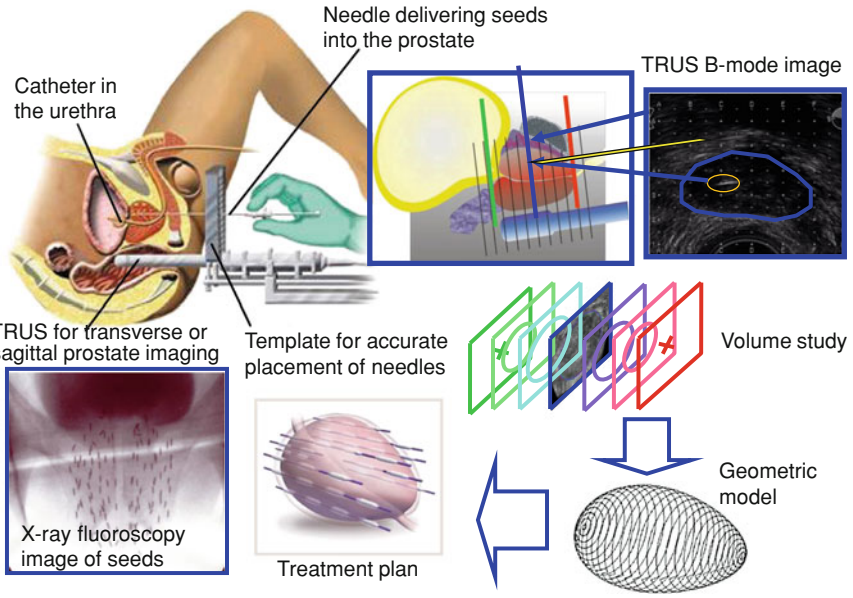


Fig. 3 Illustration of the brachytherapy procedure. The transverse TRUS image shows the needle tip artifact as the needle, shown in *yellow*, has reached this imaging plane, shown in *blue*

and the time they are kept at a specific location determines the radiation dose delivered to the prostate. The sources are removed after treatment. The treatment may involve one to several fractions. External beam radiotherapy is also used for prostate cancer treatment.

1.4 Clinical Needs

Biochemical and clinical relapse rates are low with current surgery and brachytherapy procedures. However, improvements are still required to reduce the rate of complications, which include erectile dysfunction, urinary retention, incontinence and rectal injuries. In surgery, complications are primarily associated with the tradeoff between the primary goal of the surgery—to remove all cancer—and the damaging of anatomical structures that this entails. In brachytherapy, complications have been associated with high dose loads to large portions of the prostate, with high urethral and rectal dose and with needle trauma.

These procedures, as well as the biopsy procedure, could benefit significantly from more accurate imaging of prostate cancer. If cancer could be imaged with very low false negative rates, then protocols for biopsy could be developed that would sample primarily or only suspicious regions. This would reduce the need for repeat biopsies.

More accurate cancer imaging may also allow radical prostatectomy or brachytherapy procedures to spare more healthy tissue. The goal of radical prostatectomy is to remove the entire cancer. If the specimen boundary is found to have cancerous cells, then there is a positive surgical margin, leading to a significantly higher risk of cancer recurrence. If TRUS were able to indicate with a very low false negative rate the cancerous lesions near the boundary of the prostate, a wider dissection could be made to avoid positive surgical margins. For example, if cancer were known to exist only on the right hand side of the prostate, then for surgical treatment, the left neurovascular bundle could be spared completely. Intra-operative segmentation of the prostate may also show significant benefits. If the prostate is indeed stiffer than the surrounding tissue, and studies, including our own, show that indeed it is, then more accurate segmentation of the prostate at the bladder neck and at the apex may be possible based on elasticity images. As well, the urethral stump could have differing elastic properties that could be identified.

A similar approach could be taken for brachytherapy, where the irradiated target volume could be limited to spare structures where cancer is unlikely to be found.

An increase in the accuracy of cancer imaging and its use in cancer interventions could have a significant impact on the management of the disease. The decision for immediate treatment versus active surveillance could be taken in a more educated way, and new "focal therapies" could be developed that target treatment of the largest of the identified lesions, followed by repeated imaging and biopsies to confirm disease status [14].

1.5 Elastography and its Role in Prostate Cancer Interventions

The branch of medical imaging concerned with the characterization of the mechanical properties of tissue in a non-invasive manner is called "elastography" and it has enjoyed increasing interest in the past two decades [15]. Mechanical parameters that are explored include Young's and shear moduli, viscosity, relaxation-time, Poisson's ratio and shear wave velocity.

As will be shown in the survey below, elastography shows excellent potential to improve prostate cancer imaging. Several studies have shown that prostate cancerous tissue is stiffer than normal tissue. Our own studies have also shown that the prostate itself is stiffer than the surrounding tissue, and that this fact can be used for a more reliable segmentation of the gland. Such segmentation is required for the two and three dimensional display of the prostate boundary in real time in order to ensure that the biopsy needles are placed at the desired locations. Therefore, through a better segmentation of the gland and more accurate targeting of the regions that need to be biopsied, we expect that the number of biopsy cores acquired can be reduced. In the long term, this may mean that there will be less need for repeat biopsies. Improved cancer detection can also be used in surgery

and brachytherapy to reduce damage to healthy tissue. Such damage reduction can also lead to focal therapies.

For both prostate biopsy and brachytherapy, prostate segmentation is important for gland volume estimation and for treatment planning. Because the prostate is stiffer than the surrounding tissue, it is possible to use elasticity images to improve and/or automate prostate contouring. We will present several approaches developed in our group to carry out prostate segmentation that employ deformation/elasticity images.

Deformation models can also have an important role in the registration of multi-modality images. Such registration is needed in order to provide accurate targeting of biopsies or treatment based on the best image available. To date, the most accurate detection of prostate cancer is achieved by using multi-parametric magnetic resonance images [16]. If such MRI images could be reliably registered to ultrasound during ultrasound-guided procedures, then the cancer map realized from multi-parametric MRI could be accurately superimposed against the TRUS images for more accurate targeting of tumors.

Apart from the imaging of cancer, biopsy sampling, brachytherapy and focal treatment all require that needles be placed accurately in order to collect tissue samples, or to deliver radiation or other forms of focal treatment. Needle insertion accuracy is affected by tissue deformation, as needle forces, themselves, push on the prostate and cause significant gland deflections, both in translation and rotation [17]. Therefore even if the physician aligned the TRUS perfectly according to the geometric model of the prostate, the needle may not reach the desired spatial location. Prostate brachytherapy is a procedure that is difficult to learn and to perform. We present a complete prostate brachytherapy procedure simulator based on deformation models.

2 Elastography: Basic Principles and Some Approaches

Elastography involves applying a mechanical excitation to tissue, estimating the tissue deformation from a sequence of tissue images, and finding mechanical properties of tissue that are consistent with the deformation estimates by solving an "inverse problem" of continuum mechanics.

In elastography, tissue is usually imaged with either ultrasound [18, 19], or magnetic resonance imaging, because these imaging methods do not produce ionizing radiation. Magnetic resonance elastography has been introduced by a group from the Mayo clinic in 1995 [20]. The technique has higher displacement resolution than ultrasound elastography and provides measurements of harmonic motion in three dimensions.

The mechanical excitation can be quasi-static, e.g. [19], or dynamic, e.g. [18]. The dynamic excitation can be transient, harmonic or broadband. Sources of mechanical excitation can be voice coil actuators coupled to the tissue through a rigid mechanical link [21], pneumatic [22] or hydraulic transmission [23]; manual

excitation achieved by pushing the ultrasound transducer against the tissue [15]; or internal body movement such as heart-beat or respiration. The patient's bed itself could also be made to vibrate.

A very effective way to generate tissue excitation is by using acoustic radiation forces [24]. These are generated by conventional or slightly modified ultrasound transducers that send a sequence of pulses at a high pulse repetition rate at the same focal point in tissue. The force is proportional to the ultrasound intensity and the tissue attenuation, and is inversely proportional to the speed of sound. The local tissue displacement due to this force can be computed and the resulting displacement at the focal point is measured using repeated conventional ultrasound images.

The mechanical excitation induces a tissue deformation that is described by Navier's equation. For a linear isotropic homogeneous elastic solid under the assumption of small strain and linear approximations, using Helmholtz's decomposition, the deformation can be written as the sum of two components, an "irrotational" part that is the gradient of a scalar potential function and an "equivoluminal" part that is the curl of a vector potential function. Each of the potential functions and their corresponding displacements obey wave equations. The irrotational or dilatational part corresponds to a wave equation with wave propagation speed $c_p = \sqrt{\frac{\lambda + \mu}{\rho}}$, where λ is Lamé's first parameter, μ is Lamé's second parameter and ρ is the density of the elastic solid; this speed is similar to that of the speed of sound in water (1540 m/s at 35 °C). The waves corresponding to this equation are called "primary" or longitudinal waves or "p-waves" and are sustained by elastic changes in tissue volume. The equivoluminal part corresponds to a wave equation with wave propagation speed $c_s = \sqrt{\frac{\mu}{\rho}}$; this speed is much lower than c_p, in the range from 1 to 10 m/s. The waves corresponding to this equation are called "secondary" or "shear" or "s-waves" and are sustained by elastic shearing of tissue. Shear waves are not sustained in liquids. In spite of their name which suggests that the elastic solid wave particle motion is perpendicular to the wave propagation direction, depending on boundary conditions, equivoluminal waves can, in fact, have particle motion parallel to wave propagation, and such waves have been referred to in the literature as "longitudinally polarized shear waves". In accordance with the accepted terminology within the field of elastography, we will refer to these equivoluminal waves as "shear" waves, regardless on whether they are longitudinal or not. A discussion of the issues of wave propagation in elastic solids and the influence of boundary conditions on wave speed can be found in [25, 26].

Acoustic radiation forces can be used to induce transient shear waves in elastic solids, and the speed of the shear waves can be measured using the same ultrasound machine that induces the transient wave. In "supersonic shear imaging", a sequence of acoustic radiation forces are generated in a rapid sequence along the same line at different depths. This produces a conical wave propagating from the

focal line outwards. The shear wave is imaged as it propagates and the shear modulus μ is recovered from estimates of shear wave speed c_s [27] using a parallel receive ultrasound machine that has a very high sampling rate. This approach is implemented in the Aixplorer® system (Supersonic Imagine, Aix-en-Provence, France).

In ultrasound elastography (USE), tissue motion can be estimated in real time by speckle tracking in images of raw echo data (radio-frequency or RF data). Motion can be tracked by using 1D, 2D or 3D cross-correlation [28–30]. Sub-sample resolution is achieved by interpolation of the cross-correlation function. There are many other methods for tissue motion estimation, in the time domain (zero crossing tracking, error function minimization) or in the frequency domain (phase correlation). The motion measurement resolution depends on the ultrasound wavelength, the signal to noise ratio of the echo data, and the presence of speckle. Resolution of a few microns in the axial direction is possible at conventional clinical transducer frequencies of 2–15 MHz. Lateral motion in the plane of the transducer and elevational motion orthogonal to this plane have significantly lower resolution. Such motion also degrades the axial motion estimation. The normalized cross-correlation can be used to obtain a measure of quality of the resulting displacement estimates. Conventional ultrasound machines have limited frame rates, typically between 30 and 60 Hz. For such machines, which do not have a sufficient number of acquisition channels to acquire the data in parallel, two approaches can be used to sample high frequency steady-state tissue motion. In one approach, called "sector subdivision", repeated image acquisition and motion estimation from a small sector of the ultrasound transducer image are used to generate a single sector motion map, usually described by displacement phasors. The displacement phasors corresponding to different sectors are compensated using the known delays between sector image acquisitions to generate a single consistent displacement phasor map for the entire region of interest [31, 32]. In a different approach, the "bandpass sampling" technique is used to sample band-limited motion at above twice the bandwidth of the motion, but significantly below the Nyquist rate, [33]. Thus, a signal having bandwidth between 200 and 210 Hz can be sampled at 20 Hz, fully within the capabilities of a conventional machine which could not sample at 420 Hz.

In static magnetic resonance elastography (MRE), saturation bands are applied to the magnitude images (tagged-MRI) that result in a meshed pattern of low MRI signal [34]. The displacement field is estimated from the deformation of the saturation bands. The displacements need to be larger than the spatial resolution of the image itself where the width of the saturation bands becomes a limiting factor.

In dynamic MRE, the displacements are encoded in the MR phase image using motion sensitizing gradients (MSG) with the mechanical excitation applied synchronously [35]. MSGs are superimposed on different gradient fields to encode motions in different directions. By varying the delay between the MSG and the mechanical excitation, the desired phase of the mechanical wave is acquired. The mechanical excitation can be transient (i.e., pulsed) or continuous. In continuous

dynamic MRE, the delay is stepped such that the full cycle of the mechanical motion is acquired. Depending on the application, a mechanical excitation from a few Hertz to a few kilo-Hertz can be applied. In this method, sub-micron displacements, much lower than the spatial resolution of the MR image, can be measured in tissue in clinical conditions [20]. The sensitivity of the displacement encoding depends on the performance of the gradient coils; however, the phase-to-noise ratio is the ultimate limiting factor [36].

Unless boundary conditions are known, e.g. through knowledge of the applied forces, only relative elasticity values can be calculated from static deformation measurements.

While it does not provide an absolute value of elasticity, deformation or "strain imaging" [19] provides an idea of tissue compliance. If in response to an excitation, a certain region of interest exhibits higher strain than the background, it is likely to be softer. Strain imaging is sensitive to boundary conditions and operator technique, and, in the absence of measured forces, produces only relative measurements.

In order to eliminate the operator dependence and to improve the estimates of strain imaging we can use vibro-elastography or "VE" [37], a frequency response technique in which tissue is simultaneously excited with multiple frequencies. In this approach, a time-sequence of tissue displacements is determined and used to determine a tissue transfer function relative to the transducer motion or relative to another reference, such as the motion of a particular tissue landmark. The low-frequency asymptotes of these transfer functions will be approximately inversely proportional to tissue compliance. Stiffness estimation based on transfer functions relies on elastic behavior that can be averaged over an entire low frequency range and therefore it is superior to quasi-static elastograms [37]. The phase of these transfer functions can be used to determine tissue relaxation time [38]. Associated with the transfer function computation, one can compute the "coherence function", which indicates the proportion of the input energy at a particular frequency that appears in the output at the same frequency, and therefore it is an indicator of both system linearity and signal-to-noise ratio.

There are many approaches to finding the tissue elasticity values that are consistent with the measured displacements. In general, inversion methods assume that the tissue density is constant and equal to that of water. Assuming that the measured displacements are due to shear wave propagation, and that the displacement is known as a function of time/frequency and over a region of interest, the shear wave equation can be used to find the shear modulus. In the frequency domain,

$$\rho(j\omega)^2\hat{\mathbf{u}}(x,j\omega) = \mu\nabla^2\hat{\mathbf{u}}(x,j\omega) \tag{1.1}$$

and an estimate of the displacement phasor $\hat{\mathbf{u}}(x,j\omega)$ and its Laplacian at spatial location x will yield μ if ρ and ω are known. Since second order spatial derivatives are involved, it is clear that filtering of the data is necessary for this approach to work. Optimized filter design is tackled in [39]. The Laplacian may be computed based on only one or two components depending on the specific mechanical excitation or availability of 3D or 2D data.

It has been argued in [40], that the measured displacements always contain dilatational components and that these should be removed by applying the curl operator to the displacement field.

Instead of using filtering to obtain approximate expressions for the spatial derivative, our group proposed a model fitting approach in which the derivatives are computed exactly from a specific solution form: a "Traveling Wave Expansion" of plane waves in all directions in space [41].

Alternatively, a finite element method (FEM) solution to the wave equation can be devised, and the unknown parameters of the FEM models can be solved iteratively, by minimizing an error between the measured displacements and the displacements predicted by the FEM model [42]. The FEM problem can be formulated as a "linear-in-parameters" problem which can be solved by direct inversion. In [43], a mixed FEM considering both displacements and pressures is presented. A regularizing term may be needed to deal with this poorly conditioned inverse problem, whether error minimization or direct inversion are used. Regularizing terms or a priori knowledge can be accommodated by solving a linear or a quadratic program [44]. This can be done in real time even for large problems.

For harmonic excitation, an effective approach introduced by the Mayo Clinic group who developed MRE is called the Local Frequency Estimator (LFE) [45]. This method uses filter banks to produce an estimate of the local spatial frequency.

A comparison of the methods from [43, 40, 45] on a common elastography phantom can be found in [41].

3 A Brief Survey of Prostate Elastography Imaging

The elastic properties of the prostate have been measured ex-vivo [46] by using a uniaxial indenter at 0.1, 1 and 4 Hz. The Young's modulus E for normal tissue was reported to be between 55 and 71 kPa at 2 or 4% compression, that of cancer to be higher, between 96 and 241 kPa, and benign hyperplasia lower, between 36 and 41 kPa.

In [47], prostate specimens from 15 radical prostatectomy patients were embedded in gel and were imaged with multi-compression elastograms at 0.150 mm steps, acquired as transverse scans every 2 mm, with compression achieved by a balloon around the TRUS. The study reported that the transition zone of the prostate has less strain than the peripheral zone, and it is therefore stiffer. They also found prostate cancer and benign hyperplesia tissue to be stiffer. The same group [48] showed in a study involving 31 patients that HIFU treatment stiffens the prostate, resulting in 40–60% decrease in strain in treated areas.

The earliest in-vivo elastography images of the prostate were reported in [49], using the first reported real-time elastography imaging system (Kretz Combison, later GE Voluson) [50]. The results of a much larger study (407 patients) [51], considered manual real-time elastography for guided prostate biopsy. 84% of confirmed pathological cancer cases were correctly identified by real-time

elastography as opposed to 64% with B-mode ultrasound and DRE. The study also found that chronic and acute prostatitis causes diffuse increase in elastic modulus and difficulty in forming elastograms. Specificity could not be determined by biopsy alone.

An MRE prostate study [52], using the methods of [40], found healthy prostate tissue to have Young's modulus between 6.6 and 6.9 kPa and the surrounding fat tissue 3.3 kPa at 65 Hz.

In [53], sono-elastography [18] was used to image an in-vitro prostate in 3D. Pathology, B-mode and elastography 3D images were created and registered and the image showing a vibration deficit (stiffer) correlated well with cancer.

In [54], ex-vivo prostate tissue was examined using "crawling waves". In this approach, harmonic shear waves are generated on two faces of an elastic phantom with the prostate embedded in it. The resulting shear-wave interference pattern moves slowly within the transducer imaging plane. The shear modulus is recovered from the spatial wavelength. The reported values are a factor of five lower than those reported in [46] and similar to the MRE values from [52].

In [55], stress relaxation and a Kelvin-Voigt fractional derivative model were used to correlate the ex-vivo prostate viscoelastic properties with cancer. The results show an approximate elastic contrast between the cancerous and normal tissue of 2.6:1.

In [56], 109 patients were imaged with real-time ultrasound elstography. There were 451 areas with prostate cancer, and 439 suspicious areas in elastography. Elastography had sensitivity ranging from 68 to 84% (average 75.4%) and specificity from 67 to 84% (average 76.7%), (positive predictive value of 87.8%, negative predictive value 59%) and accuracy of 76% in detecting prostate cancer, with the range of values reported depending on the specific region of the prostate considered (mid-gland, base, apex, left and right). The study also showed that with increased Gleason score both the sensitivity and specificity increase.

Higher accuracy of 92%, with sensitivity of 87%, specificity of 92%, positive predictive value of 80% and negative predictive value of 95% were reported in [57].

Acoustic radiation force impulse (ARFI) imaging of human prostates *ex-vivo* was reported in [58], showing the internal structure of the prostate, and showing that the gland lesions identified through ARFI imaging do correspond to pathology.

The ProUroScan® prostate imaging system (ProUroCare Medical Inc., Eden Prairie, Minnesota) uses a pressure array and the solution of an inverse problem to produce a volumetric stiffness map. The system was designed to assist/record DRE examinations and does not require an ultrasound machine.

From the prostate elastography studies, it results that sensitivity and specificity of elastography are significantly better than those of B-mode imaging. Apex and mid-gland images in elastography are in general better than prostate base images, and this may be due to the difficulty of inducing strain deep into the gland. It has been reported that the real-time elastography technique is difficult to learn and may

take as long as three months to use properly. This and the specific equipment use may explain some of the significant variance in the reported results. While biopsy studies are easiest to perform, a comparison of imaging with biopsy scores does not provide specificity. For that purpose, patients who undergo radical prostatectomy need to be imaged, and imaging has to be carefully registered to whole mount histopathology.

4 Prostate Vibro-Elastography Imaging

In our group we have implemented both USE and MRE systems. We will describe these in this section, provide sample images and a discussion of the results.

4.1 Ultrasound Vibro-elastography System and Images

The system utilizes a PC-based MDP machine with a biplane (transverse/sagittal) TRUS transducer (Ultrasonix Medical Corp., Richmond, BC, Canada) which is mounted on a three degree of freedom prostate imaging robot based on a commercial brachytherapy stepper (EXII; CIVCO Medical Solutions, Kalona, IA). The transducer actuation system (Fig. 4, top) has three main mechanisms: a probe cradle that can rotate the TRUS about its axis, a stage that can translate the TRUS along its axis and a vibrating stage that can translate the TRUS radially in the direction of its sagittal imaging array. All these mechanisms can be operated manually or under computer control. The original brachytherapy stepper had angle encoders that would allow the TRUS angle and depth to be read by a computer. These have been replaced with motors with encoders. The probe cradle of the original brachytherapy stepper was modified to accommodate the vibration stage which consists of a smaller holder that moves radially on a linear slider which is spring loaded against the cam of a motor (Fig. 4, top). The motor rotation angle can produce controlled radial vibration of up to 200 Hz of the TRUS probe for ultrasound elastography imaging. While the maximum displacement of the endorectal probe from its nominal center can be set by limit stops in the range 0 ± 3 mm, experimental results have shown that ± 0.5 mm is sufficient for the acquisition of prostate transfer function images.

For each RF line l, sagittal transfer functions $H_k^l(\omega)$ were generated relative to the average strain $x_{ref}(t)$ over all the RF lines $l = 1, ..., 128$, at half imaging depth, which also corresponds to the ultrasound focus depth. For each line l,

$$H_k^l(\omega) = \frac{P_{x_{ref} x_k^l}(\omega)}{P_{x_{ref} x_{ref}}(\omega)}; \qquad C_k^l(\omega) = \frac{|P_{x_{ref} x_k^l}(\omega)|^2}{P_{x_{ref} x_{ref}}(\omega) P_{x_k^l x_k^l}(\omega)} \quad . \tag{1.2}$$

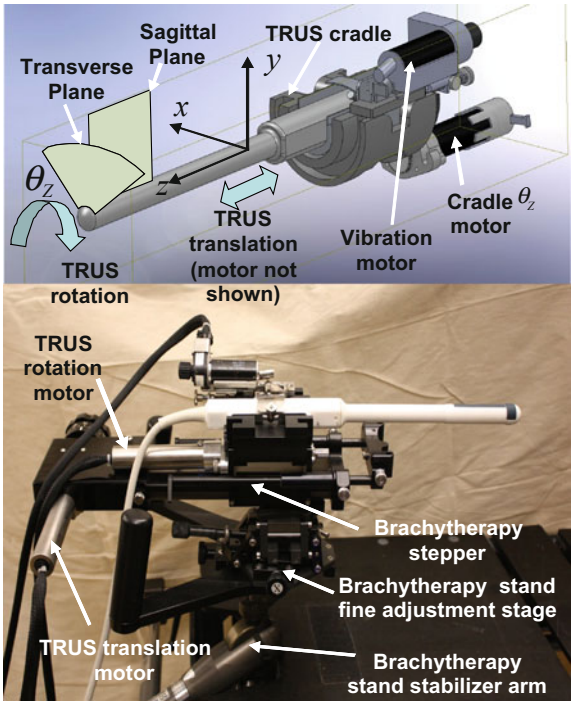


Fig. 4 VE system photo and schematic view of the TRUS probe and its cradle. The TRUS probe is mounted on a brachytherapy stepper, which can translate and rotate the TRUS. The stepper is mounted on a fine adjustment stage, which is mounted on a stabilizer arm. Both are used to position the TRUS relative to the prostate

where $P_{x_{ref}x_k^l}(\omega)$ denotes the cross spectral density between the displacement time series $x_k^l(t)$ at depth k along the line l and the reference time series $x_{ref}(t)$. The coherence function $0 < C_k^l(\omega) < 1$ is a measure of system linearity and signal to noise. It is 1 if all the input energy at one frequency appears at the output at the same frequency. The coherence function can be monitored to determine the quality of the vibro-elastography imaging.

Various phantoms have been used for validation. Images of a custom gelatin phantom [59] showed accurate identification of a stiff enclosure and its relative stiffness and coherence function close to 1 within the entire interval of excitation. Images of the Model 066 prostate elastography phantom (CIRS, Norfolk, VA) showed similar results and can be seen in Fig. 5.

Over 40 patients have been imaged to date with this approach prior to brachytherapy or radical prostatectomy, after appropriate ethics board approvals and informed patient consent. Broadband excitation from 2 to 10 Hz was used with an RF image data acquisition of approximately 40 Hz. Volume images were constructed by programming the TRUS to rotate from $-40°$ to $50°$ in increments of $2°$ with a total acquisition time of 100 s. The sagittal crystal center frequency was 5 MHz and the imaging depth was 60 mm. The RF data images were 1296 samples $\times$ 128 lines. Axial windows of 26 samples each with 50% overlap were used to compute the axial displacements using the algorithms from [28], leading to displacement time series images of 100 blocks deep by 128 lines wide.

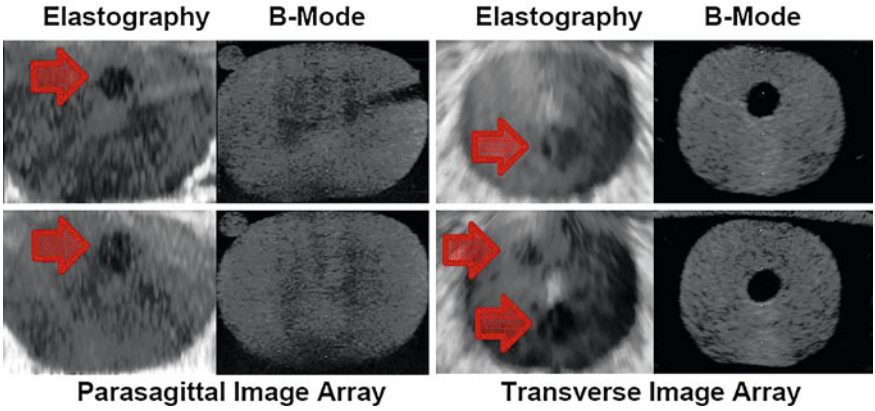


Fig. 5 Vibro-elastography and B-mode images of the CIRS 066 prostate phantom, showing stiffer enclosures

Transverse transfer function images for three patients are shown in Fig. 6. These were re-sampled from volume images obtained with the sagittal imaging array. Histogram equalization was applied to the images to improve the contrast and mean and median filtering were applied with a window size of 3×3.

4.2 Magnetic Resonance Elastography System and Images

The first in-vivo MRE images of the prostate have been reported in [52], where 65 Hz vibrations were applied to the pubic bone. Because of the mass and stiffness of the pubic bone, this approach requires high forces in order to induce shear waves in the prostate, is not always repeatable in our experience, and is uncomfortable for patients. We have implemented an alternative method which involves trans-perineal mechanical excitation (Fig. 7). In this approach, the vibration source is placed against the perineum just below the pubic bone. Unlike other methods which employ endorectal [60] or trans-urethral excitation [60], this approach is non-invasive and has been shown to be very easily tolerated by healthy volunteers and in the limited number of patients that have been imaged so far. Our initial studies were carried out with a distal electromagnetic actuator (Bruel & Kjaer Inc., Model 4808, USA), coupled from the console room to the patient perineum through a fully sealed, low pressure (<100 kPa) passive hydraulic transmission with flexurally supported "hydrospeakers" at both ends. Vibrations at 45 Hz have been used in our healthy volunteers, with a wave amplitude at the hydrospeaker distal to the actuator of approximately 1 mm peak-to-peak.

A 3T Achieva (Philips Inc., Netherlands) scanner was used with a cardiac coil. For the anatomy image a standard axial T2-weighted Fast Spin Echo sequence (echo time and repetition time ratio TE/TR = 86/2500 ms, field-of-view FOV

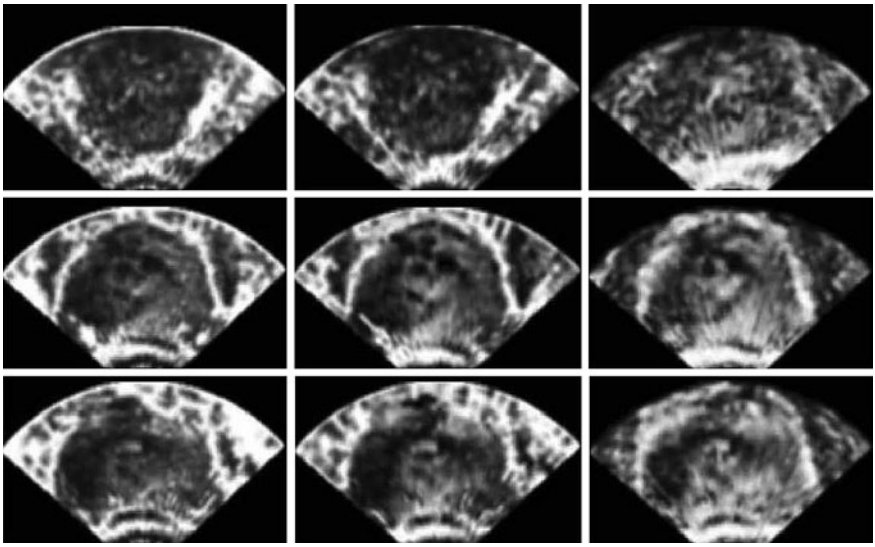


Fig. 6 Transfer function images of three brachytherapy patients (one row per patient), re-sampled from sagittal images at mid-gland

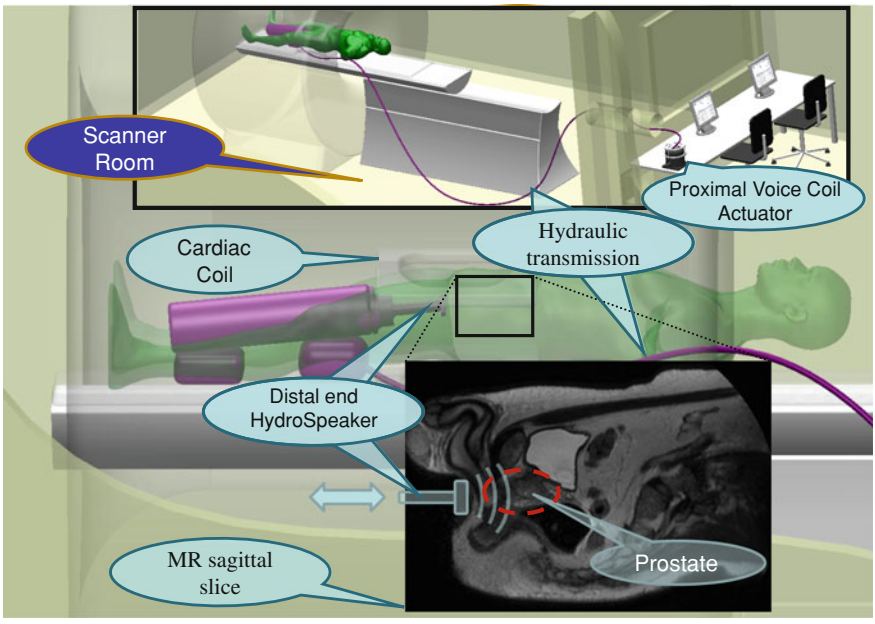


Fig. 7 MRE setup showing transperineal excitation approach

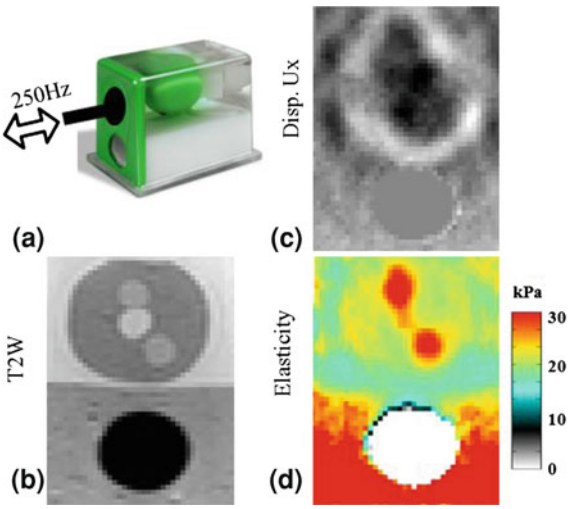


Fig. 8 Prostate phantom MRE images. **a** 250 Hz trans-perineal excitation applied to a prostate elasticity phantom using a voice-coil actuator. **b** The T2-weighted MRI image where the urethra and the two 10 mm stiffer lesions are outlined. **c** Wave component along the normal to the transverse plane. **d** Elasticity map showing the stiffer lesions

320 mm × 320 mm × 70 mm with 0.5 mm in-plane resolution and 4 mm slice thickness) was performed. The MRE images were acquired using a multi-shot Spin Echo-Echo Planar Imaging method. For the first series of subjects the wave images were acquired on a $64 \times 64 \times 7$ volume with 1.5 mm isotropic voxel size. The total imaging time for the MRE examinations was approximately 13 min (4 min per encoding direction). Two phantoms were used for validation, Model 049 quality assurance phantom and Model 066 prostate elastography phantom (CIRS Inc., Norfolk, VA). MRE images of the Model 049 phantom obtained with various reconstruction methods can be seen in [41]. Figure 8 shows a transverse plane MRE image of the Model 066 prostate phantom obtained from the volume using the method from [61]. Figure 9 shows an image acquired in a healthy 44 year-old volunteer. The elasticity image, showing elasticity of 6.1 ± 0.2 kPa, was reconstructed using local frequency estimation [45]. The damping image, showing attenuation of 6.5 ± 0.5 dB/cm was reconstructed using TWE [41]. As seen in the figure, compared to the background, the prostate gland stands out in the elastograms. Also, a close correspondence between the elasticity and T2-weighted images can be observed. A stiffer central zone and the urethra can be visually identified in Fig. 9d, e.

5 Elastography Analysis Results

An analysis of the ultrasound vibro-elastography images clearly support the superior delineation of the prostate in terms of the contrast-to-noise ratio, edge strength and edge continuity [62]. In addition, this study has also compared the volume difference and the non-overlapping volume error between the prostate

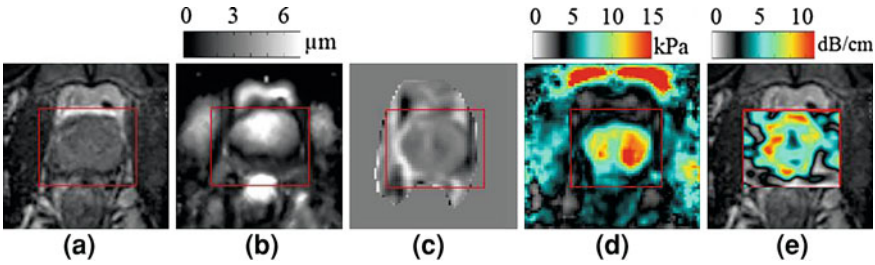


Fig. 9 MRE image of healthy volunteer acquired with the system described in Fig7. **a** Transverse prostate T2-weighted, **b** measured total wave amplitude, **c** in-plane shear waves, **d** elasticity and **e** damping in the prostate

contours estimated based on B-mode images, VE images and MRI. We found that the volume errors were marginally smaller for VE than B-mode when both are compared to MRI. Together, the volume error and the edge and contrast properties demonstrate that segmentation of the prostate in VE images is more accurate that its segmentation in B-mode images in most regions of the prostate. In addition, as can be seen in Fig. 6, VE images also show anatomical details that are not typically seen in B-mode images, such as the central zone with the urethra and the ejaculatory ducts.

To date we have analyzed the images from $N = 5$ patients who have had vibro-elastography imaging prior to radical prostatectomy and whole mount histopathology of the removed specimens. For each case, 9–13 pathology slides were extracted from the prostate at approximately 4 mm intervals and cancerous areas were marked on them. Areas suspected of cancer were marked on the VE images and then compared to the pathology results. The sensitivity of detecting the cancer in the correct region (anterior, left, right, posterior, center) of each VE slice corresponding to pathology is 75.5%. A false negative and a false positive percentage of 24.4 and 37.3% were observed, respectively. Gleason scores for 51 tumors were available. 20 of the 31 tumors with Gleason scores of $3 + 3$ (64.5%), 13 of the 16 tumors with Gleason scores of $3 + 4$ (81.25%), both tumors with Gleason scores of $4 + 3$ and both tumors with Gleason scores of $4 + 5$ were detected in VE. An example of a VE image and the corresponding whole mount pathology slice is shown in Fig. 10. The results seem to indicate, as other studies have, that the accuracy of localizing cancer improves when elastography is used as opposed to B-mode images.

5.1 Elasticity-based Segmentation

The superior contrast-to-noise of the prostate in elastography images can be used to facilitate prostate segmentation. We developed two such approaches to demonstrate feasibility, reported in [63, 64]. In [63], we used the active shape models

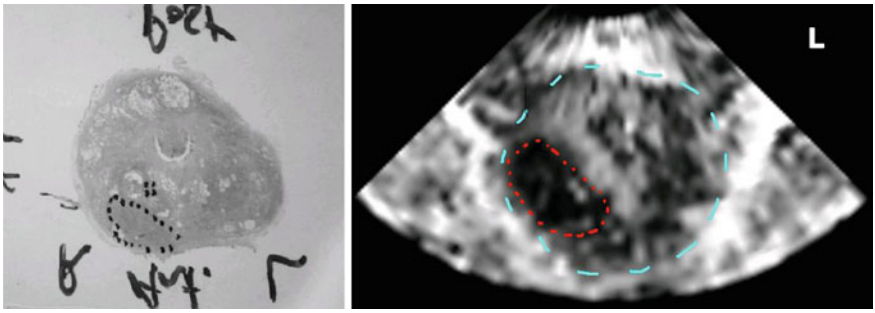


Fig. 10 Transversal images of whole mount pathology (*left*, showing a cancerous lesion with Gleason score 3 + 4), and corresponding VE image (*right*) showing the area of low strain

approach [65] to combine the high contrast between the prostate and the background in elastography with the more detailed edge information from B-mode images in order to produce fully automated segmentation of 2D prostate images. A statistical model of the prostate was created using 25 mid-gland images from 7 patients. A set of model points was created on manually segmented contours from B-mode images. The contours were aligned by iterative least-squares scaling, translation and rotation, and a mean and covariance matrix of deviations from the mean was produced. The three largest modes of variation of the covariance matrix were kept to parametrize the shape. For each of the model points, edge derivative profiles were extracted from the corresponding VE images and used to create a statistical model of the gray level appearance. The edge continuity measures were also created at the model points for both the VE and B-mode images. At each algorithm iteration, the desired deformation of the model points is computed first, by using a weighted sum of three components: a gray level similarity measure computed from the VE image, a measure of edge continuity in B-mode images and a measure of edge continuity from VE images. More weight is placed onto the gray level similarity in VE (0.5), than on the edge continuity measure in B-mode (0.25) or VE (0.25) images. While the reported errors are still fairly large, the feasibility of eliminating user input from prostate segmentation by using the VE images was demonstrated. Most of the current segmentation time for prostate radiation treatment is spent in initializing the contours [66].

In [64], a 3D automatic segmentation method for VE images was presented. Using the sagittal VE images acquired as described in Sect. 1.4, the prostate is segmented in 2D on each slice, employing the active contour method of [67]. This method employs a region-based constraint, using the variance of image pixel intensities inside/outside the contour, within a variational approach, namely the variance level-set formulation. It is stable and robust for a large range of initializations.

The segmentation starts with the central 0° sagittal slice, with the active contours method being initialized as a rectangle obtained from simple thresholding of the 1D intensity curves averaged along the image axial and lateral directions. The resulting segmentation is used to initialize the active contour method on the slices

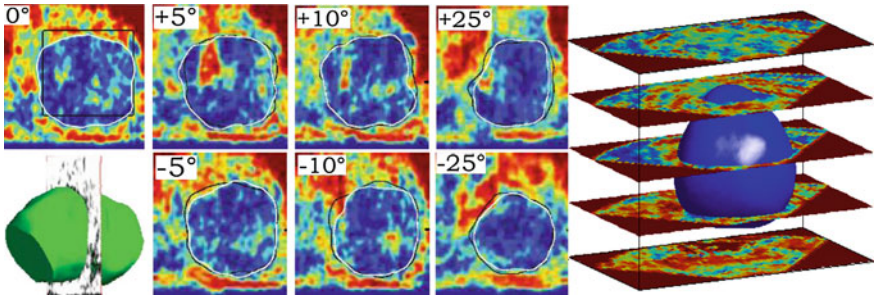


Fig. 11 VE images corresponding to the sagittal slice at $0°, \pm 5°, \pm 10°$ and $\pm 25°$. *Black* and *white curves* are initial and converged contours respectively. The final segmented 3D model is shown below the sagittal slice

at $\pm 5°$. Each subsequent pair of slices acquired at a $5°$ greater angle with the central plane is then initialized for contouring using the resulting contour of the previous image, until the entire $\pm 45°$ is traversed. When all slices are segmented, a 3D model is generated using a disc-guided shape-based interpolation technique [68]. Similarly, the prostate can also be segmented from the 3D VE volume using 3D active contours as seen on the right of Fig. 11.

An approach that uses MRE to automatically segment the prostate in MR images is presented in in [69]. We use an active contour model that evolves an initial segmentation curve until convergence. The model is a linear combination of the region-based model in [67] and the edge-based model in [70]. The region-based model is global and relies upon image statistics to partition the elasticity image into two homogeneous regions. It relies upon the high contrast of the prostate in the elasticity image, which is derived from the phase of the MRE signal. The magnitude generates an image similar to T2-weighted images. Its sharper edges are utilized by the edge-based model in order to drive the curve toward local maxima of image gradient values.

We applied the proposed algorithm to 35 pairs of images and compared the automatic contours to manual segmentations of the T2-weighted images. The resulted mean absolute distance between the contours was 1.8 ± 0.6 mm with a maximum distance of 5.6 ± 1.9 mm. The relative area error was $7.6 \pm 2.4\%$ and the duration of the segmentation process was 2 s per slice. Figure 12 shows the result in a healthy volunteer.

5.2 Elasticity-Based Registration

As described before, integrating pre-operative MRI into the ultrasound-based guidance systems commonly used would enable procedures to benefit from the accuracy of cancer detection in MRI, and possibly from the MRI-found anatomical landmarks. See, for example, [71]. There are many papers that deal with

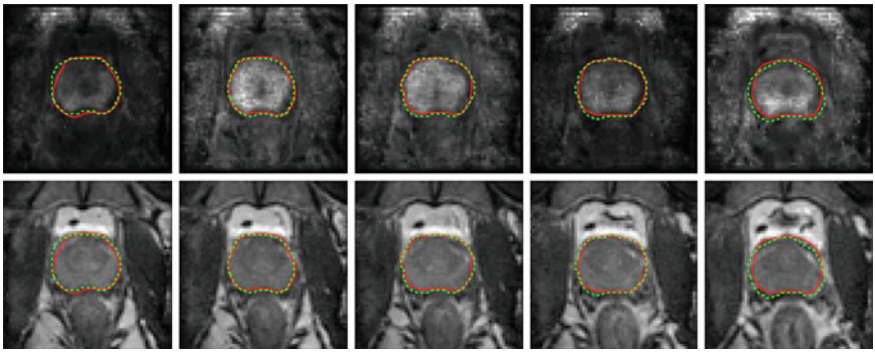


Fig. 12 Segmentation results of five slices from one patient dataset. The automatic (*solid red*) and the manual (*dashed green*) contours are overlaid on the elastograms (*top row*) and corresponding magnitude images (*bottom row*)

cross-modality registration of medical images that employ biomechanical models. For example, in [72], deformable registration between MR and TRUS is performed using a patient specific finite element statistical model.

Clearly the measured biomechanical properties of the anatomy that needs to be registered will enable more accurate deformation of one image towards the other. In addition, elasticity images that are paired up with traditional imaging protocols will enable the elasticity-based registration between images. This can be instead of, or in addition to, cross modality similarity metrics such as mutual information.

As an example of the importance that elasticity parameters and boundary forces can have for registration consider Fig. 13, which shows the registration results obtained with two finite element-based registration methods. The prostate meshes shown are from a patient who was imaged with TRUS intra-operatively during brachytherapy and with MRI post-operatively. The prostate and the urethra were manually segmented in both images (for TRUS the Foley catheter was in). The TRUS volume was modeled as a linear elastic solid with the FEM and was accordingly meshed with tetrahedral elements. The goal of the registration is to use surface forces to drive the TRUS model (source, shown in green) to the MRI surface model (target, shown in pink).

In one case, the TRUS model was driven by surface forces obtained by applying a negative pressure in the non-overlapping volume between the two surfaces. The pressure was distributed onto the nodes of the FEM model in a simulation framework to find its equilibrium state. A prostate Young's modulus of 10 kPa was assumed with a Poisson's ratio of 0.49. The result of the registration is shown in the middle of Fig. 13. The non-overlapping volume is pressurized at -1 kPa, since this results in mesh forces of the order of 10^{-1}N, which is of the same order of magnitude as the gravitational forces on the prostate.

In a second case, the method from [73] was implemented, which uses a distance map from the target surface in order to compute the FEM nodal forces. This

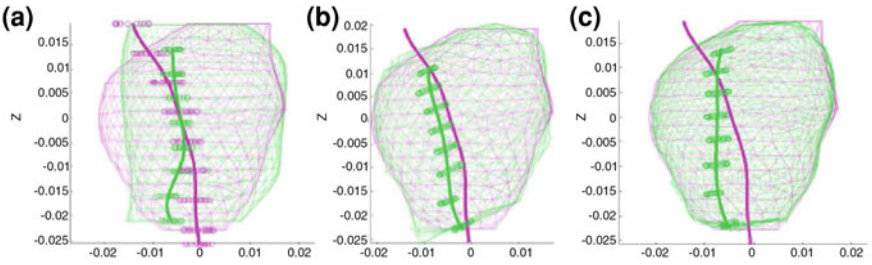


Fig. 13 Registration results for an example patient. The urethras from both the volumes are shown. **a** the unregistered surfaces, **b** the surfaces registered using [74], and **c** surfaces registered using [73]

method used the empirically set values that produced the most anatomically consistent results of Young's modulus of 30, 3 kPa and Poisson's ratio 0.2 and 0.4, for the central zone and peripheral zone, respectively.

It can be seen that even though the surface match is clearly better in Fig. 13c, the internal alignment of the urethras is better when parameters that more closely resemble the actual elasticity are employed.

To date we do not have yet absolute elastography of the same patient using both TRUS and MRE. Nevertheless, the potential of elastography-based registration can be seen in Fig. 14, where two absolute elastography images are presented on approximately the same horizontal plane through the stiff enclosures of the phantom.

The superimposed region-of-interest box shows where the ultrasound absolute elastography image is placed within the MRE image using a 2D intensity-based rigid registration. By comparison, the ultrasound and the T2-weighted MRI images show no usable contrast for the registration of these two images.

6 Deformable Models for Patient-Specific Simulation

The use of tissue elastic models for needle insertion modeling and planning has been proposed by many authors. The most complete prostate brachytherapy simulator reported to date has been developed by Goksel and Salcudean [75]. A typical view of the simulator screen is shown in Fig. 15. The system comprises the following:

- A haptic needle insertion simulator that makes use of a tissue elastic model, a flexible needle model [76], a TRUS-tissue interaction model and a needle-tissue interaction model. This system has been described in [77]. Linear FEM is used in order to allow for condensation techniques for simulation acceleration. This simulator can be easily tailored to be patient specific, as the tissue elastic model can be derived from volumetric elastography images. Furthermore, using

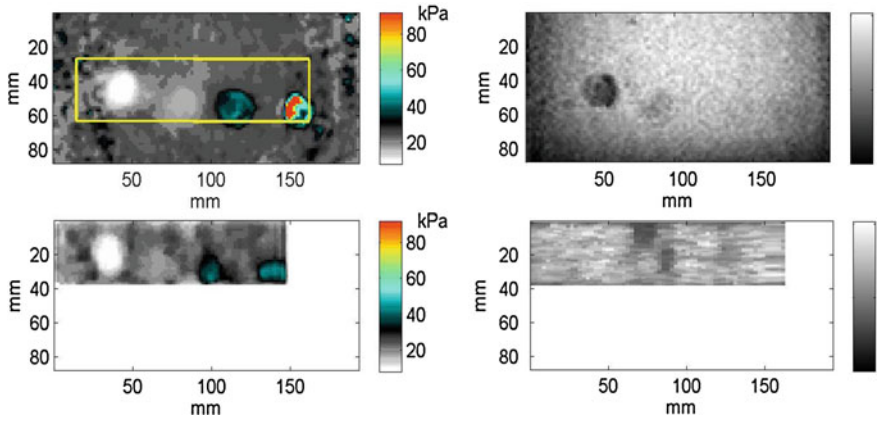


Fig. 14 MRE (*top*) and USE (*bottom*) images of a Model 049 elastography phantom. The ultrasound image of the phantom was taken by mounting a 3D US array onto a linear stage and scanning the Model 049 phantom. The imaging width is limited to the ultrasound array width (38 mm)

the mesh optimization technique described in [78], a low-order mesh that matches the anatomy, and, in particular, the shape of the prostate, can be obtained in a semi-automatic manner.

- An ultrasound tissue image simulator. This simulator uses the un-deformed ultrasound volume of the patient [79]. The planar ultrasound image of the tissue deformed as a result of needle or TRUS forces is synthesized in real time from the un-deformed volume. The mesh element to which each pixel in the synthesized ultrasound image plane belongs to when the tissue is in deformed state is obtained by solving a fast point location problem. The interpolation functions defining the pixel location within the element are used to find the intensity of the pixel form the volume prior to deformation.
- An ultrasound needle and brachytherapy seed simulator. This simulator uses interpolation from images of needles and seeds acquired in water at different locations relative to the TRUS transducer in order to generate a realistic image for a given needle or seed location [80]. The needle/seed image is then blended into the TRUS image. We have shown that the actual and synthesized images are similar using a cross-correlation based metric.

A biopsy simulator does not differ much from the above description. Indeed, the TRUS imaging direction will change to an end-firing configuration, but otherwise the exact same configuration as discussed in [77] applies.

Elastography images to feed the above simulator for specific patient cases can be acquired prior to the patient's brachytherapy by using an MRE or a TRUS elastography volume study. The MRE study is non-invasive, as no endo-rectal coil is necessary. For challenging biopsy procedures, where the patient's PSA may be rising but the biopsy results are negative, an MRI examination may be recommended

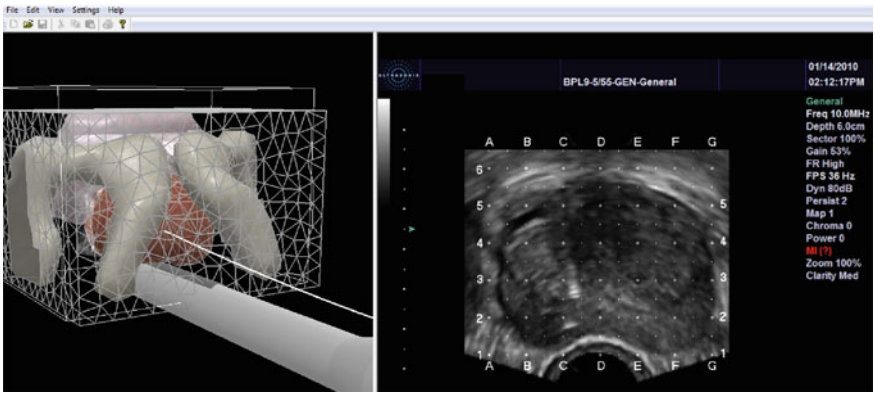


Fig. 15 Brachytherapy simulator with two panes showing the prostate anatomy (*left*) and a synthesized transverse ultrasound image corresponding to the transducer depth. Needle and seed images can be seen in the TRUS image

anyway. Indeed, the addition of the MRE protocol does not increase the acquisition time significantly with present MRI pulse sequences, and can be limited to <10 min.

In addition to procedure simulation, the simulator described above can also be used for procedure planning. This may include planning for the needle heading and puncture point assuming a rigid needle [81] and needle Jacobian-based planning [82], in which the needle base trajectory is adjusted according to the desired tip trajectory by using a needle and tissue-dependent Jacobian transformation.

Although there will continue to remain significant uncertainties in the tissue elasticity because of tissue micro-structure, nonlinear and non-isotropic effects, the largest model variability may be caused by the needle-tissue interaction model. Elastography techniques, such as tissue and needle deformation tracking, may be used in the future to refine such models. A preliminary approach using phantoms was presented in [83].

7 Conclusion

We have seen that deformation models of the prostate have important potential uses in the diagnosis and treatment of prostate cancer.

The measurement of prostate elasticity in-vivo and its correlation with histopathology is still an open research area. The studies reported to date have imaged prostate specimens or have used real-time strain imaging, not absolute elastography. Tissue frequency response over a wide bandwidth as well as tissue nonlinear response as a function of applied strain may reveal additional information that may increase the accuracy of cancer detection based on elastography.

In addition to prostate cancer imaging, prostate deformation models have uses in image registration and segmentation and can be used to simulate needle-based

procedures such as biopsy, brachytherapy and focal treatment. In simulating needle-based procedures, the largest remaining impediment is the uncertainty in the needle-tissue interaction model. Several of the steps required in prostate surgery may benefit from better prostate boundary determination and more accurate cancer imaging.

We expect rapid progress of elastography imaging in the next decade at great benefit to prostate cancer management.

Acknowledgments The authors gratefully acknowledge financial support from the Natural Sciences and Engineering Research Council of Canada, from the Canadian Institutes of Health Research and from the Natural Resources, Applied Science and Engineering program of the British Columbia Innovation Council. The prostate ultrasound elastography data was collected with partial support from the NIH. The generous support of research through the C.A. Laszlo Chair held by Professor Salcudean is gratefully acknowledged. We wish to thank Professors Robert Rohling, Dr. Jim Morris and Dr. Larry Goldenberg for collaborating with us on many aspects of the work presented in this paper.

References

1. Greene, D., Shabsigh, R., Scardino, P.: Urologic ultrasonography. In Walsh, P., Retik, A., Stamey, T., et al. (eds.) Campbell's Urology, pp.342–393, WB Saunders, PA (1992)
2. Hammerich, K., Ayala, G., Wheeler, T: Anatomy of the prostate gland and surgical pathology of prostate cancer. In: Hricak H., Scardino P. (eds.) Prostate Cancer, Cambridge University Press (2009)
3. National Cancer Institute at the National Institute of Health (NIH): Cancer Statistics, Surveillance, Epidemiology and End Results (SEER): Prostate Cancer (2011). http://seer.cancer.gov/statfacts/html/prost.html
4. Noguchi, M., Stamey, T., McNeal, J., Nolley, R.: Prognostic factors for multifocal prostate cancer in radical prostatectomy specimens: lack of significance of secondary cancers. J. Urol. **170**, 459–463 (2003)
5. Akin, O., Hricak, H.: Imaging of prostate cancer. Radiol. Clin. North Am. **45**(1), 207–222 (2007)
6. Pallwein, L., Mitterberger, M., Pelzer, A., Bartsch, G., Strasser, H., Pinggera, G., Aigner, F., Gradl, J., Nedden, D.Z., Frauscher, F.: Ultrasound of prostate cancer: recent advances. Eur. Radiol. **18**(4), 707–715 (2008)
7. Bax, J., Cool, D., Gardi, L., Knight, K., Smith, D., Montreuil, J., Sherebrin, S., Fenster, A.: Mechanically assisted 3D ultrasound guided prostate biopsy system. Med. Phys. **35**, 5397–5411 (2008)
8. Baumann, M., Mozer, P., Daanen, V., Troccaz, J.: Prostate biopsy tracking with deformation estimation. Med. Image Anal. (2011). doi:10.1016/j.media.2011.01.008
9. Fischer, G., Iordachita, I., Csoma, C., Tokuda, J., DiMaio, S., Tempany, C., Hata, N., Fichtinger, G.: MRI-compatible pneumatic robot for transperineal prostate needle placement. IEEE/ASME Trans. Mech. **13**(3), 295–305 (2008)
10. Gill, O.U.E., Desai, M.M., Steinberg, A., Kilciler, M., Ng, C.S., Abreu, S., Spaliviero, M., Ramani, A.P., Kaouk, J.H., Kawauchi, A., Miki, T.: Real-time transrectal ultrasonography during laparoscopic radical prostatectomy. J. Urol. **172**(1), 112–118 (2004)
11. Van Der Poel, H.G., de Blok, W., Bex, A., Meinhardt, W., Horenblas, S.: Peroperative transrectal ultrasonography-guided bladder neck dissection eases the learning of robot-assisted laparoscopic prostatectomy. BJU Int. **102**(7), 849–852 (2008)
12. Okihara, K., Kamoi, K., Kanazawa, M., Yamada, T., Ukimura, O., Kawauchi, A., Miki, T.: Transrectal ultrasound navigation during minilaparotomy retropubic radical prostatectomy:

impact on positive margin rates and prediction of earlier return to urinary continence. Int. J. Urol. **16**(10), 820–825 (2009)
13. Zietman, A.L.: Localized prostate cancer: brachytherapy. Curr. Treat Options Oncol. **3**(5), 429–36 (2002)
14. Eggener, S., Salomon, G., Scardino, P.T., la Rosette, J.D., Polascik, T.J., Brewster, S.: Focal therapy for prostate cancer: possibilities and limitations. Eur. Urol. **58**, 57–64 (2010)
15. Ophir, J., Cespedes, I., Garra, B., Ponnekanti, H., Huang, Y., Maklad, N.: Elastography: utrasonic imaging of tissue strain and elastic modulus in vivo. Eur. J. Ultrasound 3(1), 49–70 (1996)
16. Moradi, M., Salcudean, S.E., Chang, S.D., Jones, E.C., Buchan, N., Casey, R.G., Goldenberg, S.L., Kozlowski, P.: Multiparametric MRI maps for detection and grading of dominant prostate tumors. Magn. Reson. Imaging (2012) to appear
17. Lagerburg, V. et al.: Measurement of prostate rotation during insertion of needles for brachytherapy. Radiothera. Oncol. **77**, 318–23 (2005)
18. Lerner, R.M., Huang, S., Parker, K.J.: Sonoelasticity images derived from ultrasound signals in mechanically vibrated tissues. Ultrasound Med. Biol. **16**(3), 231–239 (1990)
19. Ophir, J., Cespedes, I., Ponnekanti, H., Yazdi, Y., Li, X.: Elastography: a qantitative method for imaging the elasticity of biological tissues. Ultrason. Imaging **13**(2) 111–134 (1991)
20. Muthupillai, R., Lomas, D., Rossman, P., Greenleaf, J., Manduca, A., Ehman, R.: Magnetic resonance elastography by direct visualization of propagating acoustic strain waves. Science **269**(5232), 1854–1857 (1995)
21. Braun, J., Braun, K., Sack, I.: Electromagnetic actuator for generating variably oriented shear waves in MR elastography. Magn. Reson. Med. **50**(1), 220–222 (2003)
22. Zheng, Y., Li, G., Chen, M., Chan, Q., Hu, S., Zhao, X., Ehman, R., Lam, E., Yang, E.: Magnetic resonance elastography with twin pneumatic drivers for wave compensation. In: Engineering in Medicine and Biology Society, 2007, EMBS 2007, 29th Annual International Conference of the IEEE, pp. 2611 –2613 (2007)
23. RS, Sahebjavaher, R, Sinkus, S.S.: Trans-perineal prostate MRE at 3T. In: Proceedings Ninth International Conference Ultrasonic Measurement and Imaging of Tissue Elasticity, Snowbird, Utah, p34 (2010)
24. Nightingale, K.R., Palmeri, M.L., Nightingale, R.W., Trahey, G.E.: On the feasibility of remote palpation using acoustic radiation force. J. Acoust. Soc. Am. **110**(1), 625–634 (2001)
25. Baghani, A., Salcudean, S., Rohling, R.: Theoretical limitations of the elastic wave equation inversion for tissue elastography. J. Acoust. Soc. Am. **126**(3), 1541–1551 (2009)
26. Eskandari, H., Baghani, A., Salcudean, S.E., Rohling, R.: The influence of the boundary conditions on longitudinal wave propagation in a viscoelastic medium. Phys. Med. Biol. **54**(13), 3997 (2009)
27. Bercoff, J., Tanter, M., Fink, M.: Supersonic shear imaging: a new technique for soft tissue elasticity mapping. IEEE Trans. Ultrason. Ferroelectr. Freq. Control **51**(4), 396–409 (2004)
28. Zahiri-Azar, R., Salcudean, S.: Motion estimation in ultrasound images using time domain cross correlation with prior estimates. IEEE Trans. Biomedical Eng. **53**(10), 1990–2000 (2006)
29. Zahiri-Azar, R., Goksel, O., Salcudean, S.: Sub-sample displacement estimation from digitized ultrasound RF signals using multi-dimensional polynomial fitting of the cross-correlation function. IEEE Trans. Ultrason. Ferroelectr. Freq. Control **57**(11), 2403–2420 (2010)
30. Pospisil, E., Rohling, R., Azar, R., Salcudean, S.: 4-D x 3-D ultrasound: real-time scan conversion, filtering, and display of displacement vectors with a motorized curvilinear transducer. IEEE Trans. Ultrason. Ferroelectr. Freq. Control **57**(10), 2271–2283 (2010)
31. Baghani, A., Brant, A., Salcudean, S., Rohling, R.: A high-frame-rate ultrasound system for the study of tissue motion. Ultrasonics, Ferroelectrics and Frequency Control. IEEE Trans. Ultrason. Ferroelectr. Freq. Control **57**(7), 1535–1547 (2010)
32. Zahiri-Azar, R., Baghani, A., Salcudean, S., Rohling, R.: 2-D high-frame-rate dynamic elastography using delay compensated and angularly compounded motion vectors: preliminary results. IEEE Trans. Ultrason. Ferroelectr. Freq. Control **57**(11), 2421–2436 (2010)

33. Eskandari, H., Goksel, O., Salcudean, S., Rohling, R.: Bandpass sampling of high-frequency tissue motion. IEEE Trans. Ultrason. Ferroelectr. Freq. Control **58**(7), 1332–1343 (2011)
34. Fowlkes, J. et al.: Magnetic-resonance imaging techniques for detection of elasticity variation. Med. Phys. **22**(11), 1771–1778 (1995)
35. Muthupillai, R., Ehman, R.L.: Magnetic resonance elastography. Nat. Med. **2**(5), 601–603 (1996)
36. Muthupillai, R., Rossman, P., Lomas, D., Greenleaf, J., Riederer, S., Ehman, R.: Magnetic resonance imaging of transverse acoustic strain waves. Magn. Reson. Med. **36**(2), 266–274 (1996)
37. Turgay, E., Salcudean, S., Rohling, R.: Identifying mechanical properties of tissue by ultrasound. Ultrasound Med. Biol. **32**(2), 221–235 (2006)
38. Eskandari, H., Salcudean, S., Rohling, R.: Viscoelastic parameter estimation based on spectral analysis. IEEE Trans. Ultrason. Ferroelectr. Freq. Control **55**(7), 1611–1625 (2008)
39. Oliphant, T., Manduca, A., Ehman, R., Greenleaf, J.: Complex-valued stiffness reconstruction for magnetic resonance elastography by algebraic inversion of the differential equation. Magn. Reson. Med. **45**, 299–310 (2001)
40. Sinkus, R., Tanter, M., Xydeas, T., Catheline, S., Bercoff, J., Fink, M.: Viscoelastic shear properties of in vivo breast lesions measured by MR elastography. Magn. Reson. Imaging **23**, 159–165 (2005)
41. Baghani, A., Salcudean, S., Honarvar, M., Sahebjavaher, R., Rohling, R., Sinkus, R.: Travelling wave expansion: A model fitting approach to the inverse problem of elasticity reconstruction. Medical Imaging, IEEE Transactions on **30**(8), 1555–1565 (2011)
42. Eskandari, H., Salcudean, S.E., Rohling, R., Ohayon, J.: Viscoelastic characterization of soft tissue from dynamic finite element models. Phys. Med. Biol. **53**(22), 6569–6590 (2008)
43. Park, E., Maniatty, A.M.: Shear modulus reconstruction in dynamic elastography: Time harmonic case. Phys. Med. Biol. **51**(15), 3697–3721 (2006)
44. Eskandari, H., Salcudean, S.E., Rohling, R., Bell, I.: Real-time solution of the finite element inverse problem of viscoelasticity. Inverse Problems **27**(8), 085002 (2011)
45. Manduca, A., Muthupillai, R., Rossman, P.J., Greenleaf, J.F., Ehman, R.L.: Local wavelength estimation for magnetic-resonance elastography. In: Proceedings of International Conference of Image Processing, pp. 527–530 (1996)
46. Krouskop, T.A., Wheeler, T.M., Kallel, F., Garra, B.S., Hall, T.: Elastic moduli of breast and prostate tissues under compression. Ultrason. Imaging **20**(4), 260–274 (1998)
47. Souchon R., Hervieu V., Gelet A., Ophir J., Chapelon J.Y. Human prostate elastography: in vitro study. In: 2003 IEEE Symposium on Ultrasonics, vol. 2, pp.1251–1253 (2003)
48. Souchon, R., Rouvire, O., Gelet, A., Detti, V., Srinivasan, S., Ophir, J., Chapelon, J.Y.: Visualisation of HIFU lesions using elastography of the human prostate in vivo: preliminary results. Ultrasound Med. Biol. **29**(7), 1007–1015 (2003)
49. Pesavento, A., Lorenz, A.: Real time strain imaging and in-vivo applications in prostate cancer. In: 2001 IEEE Symposium on Ultrasonics, vol. 2, pp.1647–1652 (2001)
50. Lorenz, A., Sommerfeld, H., Garcia-Schurmann, M., Philippou, S., Senge, T., Ermert, H.: A new system for the acquisition of ultrasonic multicompression strain images of the human prostate in vivo. IEEE Trans. Ultrason. Ferroelectr. Freq. Control **46**(5), 1147–1154 (1999)
51. Konig, K., Scheipers, U., Pesavento, A., Lorenz, A., Ermert, H., al., T.S.: Initial experiences with real-time elastography guided biopsies of the prostate. J. Urol. **174**, 115–117 (2005)
52. Kemper, J., Sinkus, R., Lorenzen, J., Nolte-Ernsting, C., Stork, A., Adam, G.: MR elastography of the prostate: initial in-vivo application (in german - MR-elastographie der prostata: erste in-vivo-anwendung. Rofo. Fortschritte auf dem Gebiet der Rontgenstrahlen und der bildgebenden Verfahren **176**, 1094–1099 (2004)
53. Taylor, L.S., Rubens, D.J., Porter, B.C., Wu, Z., Baggs, R.B., di Sant'Agnese, P.A., Nadasdy, G., Pasternack, D., Messing, E.M., Nigwekar, P., Parker, K.J.: Prostate cancer: three-dimensional sonoelastography for in vitro detection. Radiol. **237**(3), 981–985 (2005)
54. Zhang, M., Castaneda, B., Wu, Z., Nigwekar, P., Joseph, J.V., Rubens, D.J., Parker, K.J.: Congruence of imaging estimators and mechanical measurements of viscoelastic properties of soft tissues. Ultrasound Med. Biol. **33**(10), 1617–1631 (2007)

55. Zhang, M., Nigwekar, P., Castaneda, B., Hoyt, K., Joseph, J.V., di Sant'Agnese, A., Messing, E.M., Strang, J.G., Rubens, D.J., Parker, K.J.: Quantitative characterization of viscoelastic properties of human prostate correlated with histology. Ultrasound Med. Biol. **34**(7), 1033–1042 (2008)
56. Salomon, G., Köllerman, J., Thederan, I., Chun, F.K., Budäus, L., Schlomm, T., Isbarn, H., Heinzer, H., Huland, H., Graefen, M.: Evaluation of prostate cancer detection with ultrasound real-time elastography: a comparison with step section pathological analysis after radical prostatectomy. Eur. Urol.**54**(6), 1354–1362 (2008)
57. Pallwein, L.M., Michael Struve, P., Pinggera, G., Horninger, W., Bartsch, G., Aigner, F., Lorenz, A., Pedross, F., Frauscher, F.: Real-time elastography for detecting prostate cancer: preliminary experience. BJU Int. **100**(1), 42–46 (2007)
58. Zhai, L., Madden, J., Foo, W.C., Palmeri, M.L., Mouraviev, V., Polascik, T.J., Nightingale, K.R.: Acoustic radiation force impulse imaging of human prostates ex vivo. Ultrasound Med. Biol.**36**(4), 576–588 (2010)
59. Salcudean, S., French, D., Bachmann, S., Zahiri-Azar, R., Wen, X., Morris, W.: Viscoelasticity modeling of the prostate region using vibro-elastography. In: Larsen, R., Nielsen, M., Sporring, J. (eds.): Medical Image Computing and Computer-Assisted Intervention MICCAI 2006. Volume 4190 of Lecture Notes in Computer Science, vol. 4190, pp. 389–396. Springer Berlin (2006) doi: 10.1007/11866565_48
60. Arani, A., Plewes, D., Krieger, A., Chopra, R.: The feasibility of endorectal MR elastography for prostate cancer localization. Magn. Reson. Med. (2011) 1649–1657
61. Sinkus, R., Lorenzen, J., Schrader, D., Lorenzen, M., Dargatz, M., Holz, D.: High-resolution tensor MR elastography for breast tumour detection. Phys. Med. Biol. **45**(6), 1649 (2000)
62. Mahdavi, S.S., Moradi, M., Wen, X., Morris, W.J., Salcudean, S.E. Evaluation of visualization of the prostate gland in vibro-elastography images. Med. Image Anal. **15**(4), 589 – 600 (2011)
63. Mahdavi, S., Moradi, M., Morris, W., Salcudean, S.: Automatic prostate segmentation using fused ultrasound B-mode and elastography images. In Jiang, T., Navab, N., Pluim, J., Viergever, M., eds.: Medical Image Computing and Computer-Assisted Intervention MICCAI 2010. Volume 6362 of Lecture Notes in Computer Science, pp. 76–83. Springer Berlin (2010)
64. Goksel, O., Salcudean, S.: Automatic prostate segmentation from transrectal ultrasound elastography images using geometric active contours. In: Proceedings of the Eighth International Conference on the Ultrasonic Measurement and Imaging of Tissue Elasticity, Vlissingen, Zeeland, The Netherlands (2009)
65. Cootes, T., Taylor, C., Cooper, D., Graham, J.: Active shape models-their training and application. Comput. Vis. Image Underst. **61**(1), 38–59 (1995)
66. Mahdavi, S.S., Chng, N., Spadinger, I., Morris, W.J., Salcudean, S.E.: Semi-automatic segmentation for prostate interventions. Med. Image Anal. **15**(2), 226–237 (2011)
67. Chan, T., Vese, L.: Active contours without edges. IEEE Trans. Image Process. **10**(2), 266–277 (2001)
68. Treece, G., Prager, R., Gee, A., Berman, L.: Surface interpolation from sparse cross sections using region correspondence. IEEE Trans. Med. Imaging **19**(11), 1106–1114 (2000)
69. Nir, G., Baghani, A., Sahebjavaher, R.S., Sinkus, R., Salcudean, S.E.: A combined region-edge-based approach to segmentation of the prostate in magnetic resonance elastography. In: Proceedings of the Tenth International Conference on the Ultrasonic Measurement and Imaging of Tissue Elasticity, Arlingto, TX (2011)
70. Caselles, V., Kimmel, R., Sapiro, G.: Geodesic active contours. Int. J. Comput. Vis. **22**, 61–79 (1997)
71. Reynier, C., Troccaz, J., Fourneret, P., Dusserre, A., Gay-Jeune, C., Descotes, J.C., Bolla, M., Giraud, J.Y.: MRI/TRUS data fusion for prostate brachytherapy: preliminary results. Med. phys. **31**, 1568 (2004)
72. Hu, Y., Ahmed, H.U., Taylor, Z., Allen, C., Emberton, M., Hawkes, D., Barratt, D.: MR to ultrasound registration for image-guided prostate interventions. Med. Image Anal. **103**(2–3), (2010) to appear

73. Bharatha, A., Hirose, M., Hata, N., Warfield, S., Ferrant, M., Zou, K., Suarez-Santana, E., Ruiz-Alzola, J., DAmico, A., Cormack, R., Kikinis, R., Jolesz, F.A., Tempany, C.M.C.: Evaluation of three dimensional finite element-based deformable registration of pre-and intraoperative prostate imaging. Med. phys. **28**, 2551 (2001)
74. Taquee, F., Goksel, O., Mahdavi, S.S., Keyes, M., Morris, W.J., Spadinger, I., Salcudean, S.E.: Deformable prostate registration from mr and trus images using surface error driven fem models. In: Proceedings of SPIE (2012)
75. Goksel, O., Salcudean, S.E.: Haptic simulator for prostate brachytherapy with simulated ultrasound. In: International Symposium on Biomedical Simulation (ISBMS), pp. 150–159 (2010)
76. Goksel, O., Dehghan, E., Salcudean, S.E.: Modeling and simulation of flexible needles. Med. Eng. Phys. **31**(9), 1069–1078 (2009)
77. Goksel, O., Sapchuk, K., Salcudean, S.: Haptic simulator for prostate brachytherapy with simulated needle and probe interaction. Haptics. IEEE Trans. Haptics **4**(3), 188–198 (2011)
78. Goksel, O., Salcudean, S.E.: Image-based variational meshing. IEEE Trans. Med. Imaging **30**(1), 11–21 (2011)
79. Goksel, O., Salcudean, S.E.: B-mode ultrasound image simulation in deformable 3-D medium. IEEE Trans. Med. Imaging **28**(11), 1657–1669 (2009)
80. Zhu, M., Salcudean, S.: Real-time image-based B-mode ultrasound image simulation of needles using tensor-product interpolation. IEEE Trans. Med. Imaging **30**(7), 1391–1400 (2011)
81. Dehghan, E., Salcudean, S.: Needle insertion parameter optimization for brachytherapy. IEEE Trans. Robotics **25**(2), 303–315 (2009)
82. DiMaio, S., Salcudean, S.: Needle steering and motion planning in soft tissues. IEEE Trans. Biomedical Eng. **52**(6), 965–974 (2005)
83. Dehghan, E., Wen, X., Zahiri-Azar, R., Marchal, M., Salcudean, S.E.: Needle-tissue interaction modeling using ultrasound-based motion estimation: phantom study. Comput. Aided Surg. **13**(5), 265–280 (2008)